IEEE Access
Multidisciplinary ⋮ Rapid Review ⋮ Open Access Journal

Received January 5, 2022, accepted January 21, 2022, date of publication January 26, 2022, date of current version February 10, 2022.

Digital Object Identifier 10.1109/ACCESS.2022.3146722

Grounding Grid Fault Diagnosis With Emphasis on Substation Electromagnetic Interference

AAMIR QAMAR[1], IBRAHIM H. AL-KHARSAN[2], ZAHOOR UDDIN[1], AND AHMED ALKHAYYAT[2]

[1]Department of Electrical and Computer Engineering, COMSATS University Islamabad, Wah Campus, Rawalpindi 47040, Pakistan
[2]Department of Computer Technical Engineering, College of Technical Engineering, Islamic University, Najaf 54001, Iraq

Corresponding author: Aamir Qamar (aamirqamar@ciitwah.edu.pk)

ABSTRACT Grounding grid fault diagnosis is essential for the safe operation of a substation. However, the substation vicinity is highly electromagnetic. Therefore, the electromagnetic-based fault diagnosis is vulnerable to electromagnetic interference (EMI). This paper presents the gradient electromagnetic method for the grounding grid fault diagnosis but unlike the previous methods, fault diagnosis here includes the breakpoints and percentage corrosion simultaneously. The diagnosis is based on comparing the calculated resistivity with the designed resistivity of the grid. The resistivity is calculated from the grid's surface electric and magnetic fields. Furthermore, the existing literature, emphasis on EMI is negligible with the main focus on fault diagnosis only. Therefore, to cope with the EMI, we utilized the Independent Vector Analysis (IVA) to isolate the grounding grid signal from the interfered signal. The validity of IVA is examined by comparing with different known isolation algorithms considering various evaluation criteria. The mathematical reasoning, simulation results and experimental output illustrate that the gradient electromagnetic method along the IVA is feasible for grounding grid fault diagnosis under substation electromagnetic environment (EME).

INDEX TERMS Electromagnetic field, EMI, fault diagnosis, grounding grid, IVA.

I. INTRODUCTION

Grounding grids in substations are installed to ensure the power system's safety and reliability. It is the sole responsibility of the grounding grid to discharge hazardous currents into the earth in case of lightning strokes and faults [1]–[3]. Most grounding grids are made up of copper, steel, galvanized steel, etc. The working of grounding grid under the moist conditions of soil significantly causes corrosion and even breaks. This degrades the performance of the grounding grid that directly jeopardizes the safety of the power system and workers. Therefore, it is important to develop effective fault diagnosis techniques to regularly monitor the status of the grounding grid without excavation and power disruption.

The literature on the fault diagnosis of grounding grid is classified into three categories: electric network methods [4]–[7], electrochemical detection methods [8]–[10] and electromagnetic methods [11]–[15]. In electric network methods, the grounding grid is treated as a resistive network and measures the port resistance of the vertical conductor to calculate the branch resistance. The corrosion status is determined by comparing the calculated branch resistance with the design value. The electric network methods are ineffective as they can only diagnose corrosion and no breakpoints. Furthermore, the change in grounding resistance is quite small even if the grid is fractured. Electrochemical methods work by measuring electrochemical properties between soil and grounding grid. These methods are quite effective to diagnose corrosion levels but fail to detect breakpoints. Furthermore, the electrical impedance tomography (EIT) is used in [16] to image the corrosion in the grounding grid. The data points in this method are low but the potential measurement at the downlead wires is a major shortcoming of this method. Since the downlead wire is not connected at each node of the grid, therefore, to get more node potentials the cycle measurement is utilized [17]. This method is also tedious as it utilizes the Tikhonov regularization to weaken the ill-posedness of the inverse problem.

Electromagnetic (EM) methods are classified as current injection methods [11]–[13], [18] and transient electromagnetic methods [14], [15], [19]. EM methods are aimed to induce current in the grid. As a result, the magnetic field at

The associate editor coordinating the review of this manuscript and approving it for publication was Akshay Saha.

the surface is measured and processed. I.e, Zhang *et al.* [11] measured the surface potential difference taking the frequency characteristics of soil and grounding conductors into account to diagnose faults in a grounding grid. In [12], the authors diagnosed faults in grounding grid using magnetic detection electric impedance tomography (MDEIT). In this method the surface magnetic flux density generated from the current injection is subjected to inversion calculations to obtain electric resistivity. The faults in the grounding grid are diagnosed from the electric resistivity distribution. The main shortcoming of this method is the enormous number of measurements. In [13], derivative method is used to diagnose breakpoints in the grounding grid. Gradient peak of magnetic flux density at conductor's location shows normal conductor while no peak at conductor location confirms broken conductor. Derivative method fails in the presence of strong electromagnetic environment (EME) as it enhances the magnetic field of substation along with the magnetic field of grounding grid. Moreover, the authors of [18], utilized the electrical resistance tomography (ERT) to diagnose leaks from buried pipes. Electrodes were used to inject current and measure the potential drop at the earth's surface using dipole-dipole and an updated Schlumberger array. In [14], [15], [19], transient electromagnetic method (TEM) is used to diagnose breakpoints. In this method the faults are diagnosed using equivalent resistivity distribution that is calculated from the secondary magnetic field of the grounding grid using optimization technique. This method fails as it cannot distinguish an absent conductor from the one that is broken.

Distribution substation comprises of multiple equipment such as power transformers, circuit breakers, instrument transformers, conductors, busbars, grounding grid, etc. Therefore, the substation surrounding is intensely electromagnetic. In such strong electromagnetic environment (EME), utilizing electromagnetic methods for fault diagnosis of grounding grid are subjected to electromagnetic interference (EMI) [20]. The existing techniques concentrate only on fault detection with minimum consideration to EMI. This is why the electromagnetic method for fault diagnosis must be accompanied by methods to curb the EMI.

The Independent Component Analysis (ICA) is often used to isolate the sources electroencephalogram (EEG) signals in a multi-channel EEG signals where they are mixed with the electrooculogram and electromyogram signals [21].

The ICA is also used to curb EMI for the inverse features identification of the grounding grid [22] but the inefficiency of ICA is reported in [23] and [24]. In literature, Canonical Correlation Analysis (CCA) is used as an alternative to ICA [25]. CCA utilizes the original signals as well as the delayed versions of the signals. It is based on the second order statistics (SOS) and extract maximally auto-correlated and mutually un-correlated signals [25]. From [26], it is known that CCA is an efficient and practically use-able technique as compared to ICA. Moreover, ICA utilizes higher order statistics (HOS) to explore statistical independence while CCA is based on SOS to recover statistically un-correlated sources. It is clear from the statistical theory that un-correlatedness is a weaker condition than independence. The independent vector analysis (IVA) combines the advantages of both ICA and CCA in a single framework [27]. IVA processes the original and time delayed versions of the signals while utilizing the HOS. IVA assumes that the source signals in one data set are independent to each other and at least one source is dependent on one source of the other data set. Moreover, from [27] it is known that IVA performs well as compare to ICA and CCA.

This paper proposes gradient and independent vector analysis (IVA) techniques to diagnose faults in the grounding grid under a substation strong EME. Unlike the previous literature, the proposed gradient approach for grounding grid fault diagnosis incorporates the break-point and corrosion diagnosis simultaneously. Furthermore, the proposed method diagnose corrosion in a grounding grid by directly calculating the resistance of each grounding conductor that unlike the previous resistance calculation methods optimizes it. This paper also, considers the substation EME that falsifies the results of electromagnetic approach. Therefore, we propose IVA to separate the source signal from the interfered signal. Moreover, this paper is the first to introduce the IVA based technique for grounding grid fault diagnosis as well as the first to diagnose the faults accounting the EME of the substation. The IVA based technique produces more accurate signals that might help to observe some very low amplitude signals. We utilized the well known algorithm of IVA called the IVA-L for blind separation of the recorded mixed signals [28]. The proposed technique is reliable and practically applicable due to its effectiveness against EMI sources. However, the proposed method does demand the prior knowledge of the layout and depth of a grounding grid, the factors that varies both during construction and over time [12], [22], [29]. Mathematical reasoning, simulation results and experimental tests validate the feasibility of the proposed method for grounding grid fault diagnosis under substation EMI.

II. GROUNDING CONDUCTOR STATUS INVESTIGATION

A grounding conductor of infinite length stationed along y-axis is illustrated in Fig. 1. This conductor is buried at depth h in a homogeneous soil of permeability μ and carries direct current I. According to Ampere's law the magnetic flux density at point P on the ground surface that surrounds the conductor is $\vec{B_\phi}$. Mathematically $\vec{B_\phi}$ is expressed as:

$$\vec{B_\phi} = \frac{\mu I}{2\pi R}\hat{a_\phi} \tag{1}$$

The $\hat{a_\phi}$ in (1) is the unit vector representing the direction of $\vec{B_\phi}$ and R is the distance between the conductor and point P. Expressing $\vec{B_\phi}$ in terms of Cartesian coordinates is given as:

$$\vec{B_x} + \vec{B_z} = \frac{\mu I}{2\pi R}\left(cos\phi\hat{a_x} - sin\phi\hat{a_z}\right) \tag{2}$$

$$\vec{B_x} = \frac{\mu I}{2\pi}\frac{h}{x^2 + h^2}\hat{a_x} \tag{3}$$

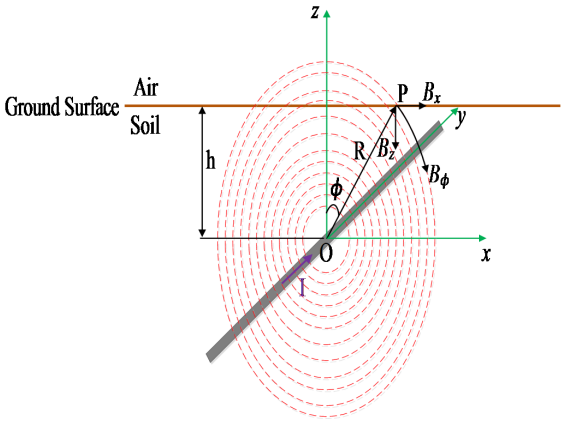

FIGURE 1. Magnetic flux density $\vec{B}_\phi$ produced from an infinite length grounding conductor carrying current I. This conductor is stationed along y-axis and buried at depth h below the earth surface.

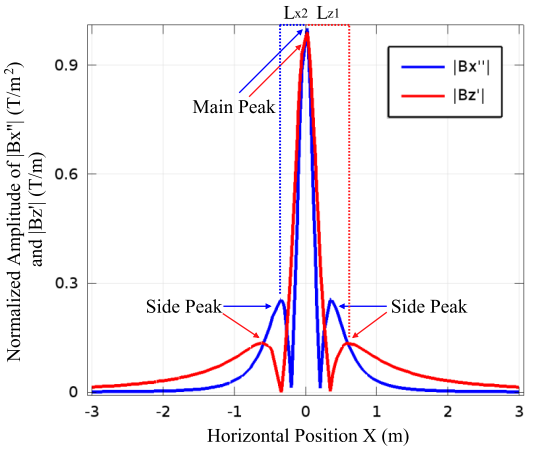

FIGURE 2. 2^{nd} order gradient modulus of $\vec{B}_x$ and 1^{st} order gradient modulus of $\vec{B}_z$. Conductor location is confirmed by the position of main peak at x=0m.

$$\vec{B}_z = -\frac{\mu I}{2\pi}\frac{x}{x^2+h^2}\hat{a}_z \tag{4}$$

In x-direction the 2^{nd} order gradient modulus of (3) and 1^{st} order gradient modulus of (4) is presented as:

$$|\vec{B}_x{}''| = |\frac{\mu I h}{\pi} \times \frac{3x^2-h^2}{\left(x^2+h^2\right)^3}|\hat{a}_x \tag{5}$$

$$|\vec{B}_z{}'| = |\frac{\mu I}{2\pi} \times \frac{x^2-h^2}{\left(x^2+h^2\right)^2}|\hat{a}_z \tag{6}$$

Analyzing (5) and (6), $|\vec{B}_x{}''|$ and $|\vec{B}_z{}'|$ are maximum at x=0m that resembles the location of the conductor below the earth surface. The graphical representation of (5) and (6) is illustrated in Fig. 2. Main peak of $|\vec{B}_x{}''|$ and $|\vec{B}_z{}'|$ is positioned at x=0m that is in accordance with the mathematical result.

The presence of magnetic flux density gradient peak shows a normal conductor carrying the current. On the other hand, if the conductor is broken the flow of current is absent that will result in no peak. However, to diagnose corroded conductor or to calculate the percentage of conductor corroded, current in the conductor is calculated.

According to [29], the burial depth of the conductor for the case of $\vec{B}_x$ and $\vec{B}_z$ is expressed as:

$$h \approx L_{x2} \tag{7}$$

$$h \approx 0.5774 L_{z1} \tag{8}$$

The L_{x2} and L_{z1} are the distances between the main peak and side peak of $|\vec{B}_x{}''|$ and $|\vec{B}_z{}'|$. According to (5) and (6), employing the limit at x=0 results in current I that is expressed as:

$$I = \lim_{x\to 0} |\vec{B}_x{}''| \frac{\pi h^3}{\mu} \tag{9}$$

$$I = \lim_{x\to 0} |\vec{B}_z{}'| \frac{2\pi h^2}{\mu} \tag{10}$$

A. PERCENTAGE OF CONDUCTOR CORROSION

In order to calculate the percentage of conductor corrosion, the conductivity of the conductor is calculated based on Ohm's law:

$$\sigma_c = \frac{IL}{VA} \tag{11}$$

The I is the current flowing in the conductor, L is the length of conductor, A is its cross sectional area and V is the potential drop across the conductor. L and A are the conductor's designed parameters while I is calculated using (9) and (10). Finally, V is calculated from the electric field intensity $\vec{E}$ measured at the earth surface. As the dc current flows along the conductor, $\vec{E}$ remains uniform. Therefore, the voltage drop across the conductor is expressed as:

$$V = \vec{E} \cdot \vec{L} \tag{12}$$

The percentage corrosion is expressed as:

$$\%_{corrosion} = \frac{\sigma_d - \sigma_c}{\sigma_d} \times 100 \tag{13}$$

The σ_d is the designed conductivity of the conductor.

As the substation surrounding is highly electromagnetic (EM), the measured data is mixed signals comprising source (grounding grid) signal and surrounding EM signals. Applying the gradient approach to the raw measurement will enhance the noise (EMI). Therefore, to overcome the problem of EMI, the IVA technique is utilized to separate the source signal from the mixed recorded signal before the gradient approach is applied. The system model of IVA is discussed in Section III-A.

The surrounding of substation is highly electromagnetic due to the presence of electromagnetic equipment such as transformers, bus bars, etc. Therefore, the gradient of raw measurements to diagnose faults in grounding grid is unpractical that will result in perverted results.

The behavior of EM signal from various instruments in a substation is different but due to the IVA being a blind

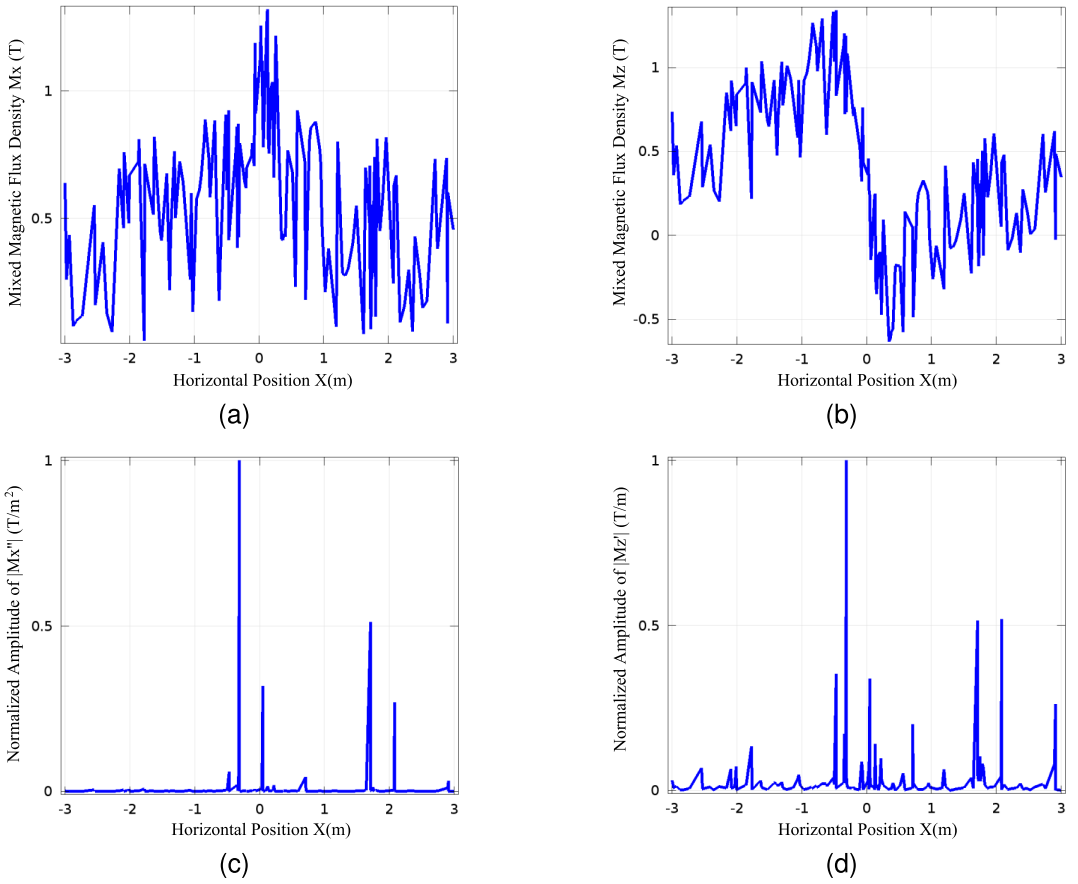

FIGURE 3. Influence of EME on the magnetic flux density gradient. Fake peaks emerged compelling the identification of true peaks impossible. (a) Mixed magnetic flux density $\vec{M}_x$ is obtained by mixing $\vec{B}_x$ with the Matlab generated EME environment. (b) Mixed magnetic flux density $\vec{M}_z$ is obtained by mixing $\vec{B}_z$ with the Matlab generated EME environment. (c) Normalized 2^{nd} order gradient modulus of $\vec{M}_x$. (d) Normalized 1^{st} order gradient modulus of $\vec{M}_z$.

source separation technique, it is independent of the EMI behavior. Although, the number of IVA sensors must be equal to the number of EM signals. IVA being independent of EMI behavior, the influence of EME on the gradient of grounding conductor magnetic flux density is illustrated by considering the EMI as a single electromagnetic signal (EMS) that is mixed with $\vec{B}_x$ and $\vec{B}_z$ each. This is illustrated in Fig. 3a and 3b. Afterwards, the 2^{nd} order gradient of the mixed signal $\vec{M}_x$ and 1^{st} order gradient of the mixed signal $\vec{M}_z$ is illustrated in Fig. 3c and 3d. The gradient results show multiple peaks. This is because the EMS is also enhanced with the grounding conductor magnetic flux density. In current state, the identification of the true peak corresponding to the grounding conductor is impossible. To combat the problem of EME, the IVA technique is utilized to separate the original signal from the mixed signal before the gradient process.

III. INDEPENDENT VECTOR ANALYSIS

Independent vector analysis is one of the Blind Source Separation techniques (BSS) that utilizes higher order statistics (HOS) to separate the source signal from the mixed signal. The conceptual model of IVA is illustrated in Fig. 4.

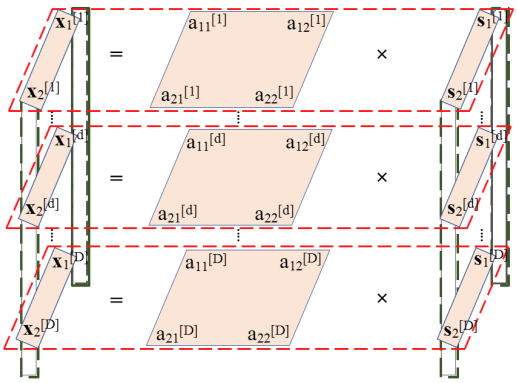

FIGURE 4. Conceptual model of Independent Vector Analysis (IVA). $\mathbf{x}_1$ and $\mathbf{x}_2$ illustrate the vectors of mixed recorded signals, $a_{11} \cdots a_{22}$ are the elements of mixing matrix and $\mathbf{s}_1$ and $\mathbf{s}_2$ are the transmitted signal vectors. $^{[1]} \ldots ^{[D]}$ are the superscripts illustrating directly transmitted and reflected signals data sets.

In this figure, $\mathbf{x}_1$ and $\mathbf{x}_2$ represent the vectors of mixed recorded signals, $a_{11} \cdots a_{22}$ represent mixing matrix elements and $\mathbf{s}_1$ and $\mathbf{s}_2$ represent the transmitted signal vectors. The

received signals by the sensors contain directly transmitted and reflected signals. Therefore, the superscript $^{[1]}$ represents the data of directly transmitted and $^{[D]}$ represents the data set of reflected signals. The superscript $^{[d]}$ is meant for a general data set.

A. IVA SYSTEM MODEL

This sub-section presents the grounding grid and the EMI signals in the IVA data model. Let the number of independent source signals be K i.e., grounding grid and EMI signals. All the sources contain L number of samples for D data sets. The acquired data through sensors is represented as follows:

$$X^d = A^d S^d \quad 1 \leq d \leq D, \tag{14}$$

The S^d contains source data vectors $s_1^d, s_2^d, \ldots, s_k^d$, each of length L. Each source data vector contains real random values with zero mean data. A^d represents real valued random mixing matrices for D data sets. Here, the role of the IVA algorithm is to estimate the unknown mixing matrices for the recorded data. The source data matrices in different data sets are represented by $(S^1)^T, (S^2)^T, \ldots, (S^D)^T$. After estimating all the mixing matrices the IVA post processed data is expressed as:

$$Y^d = W^d X^d \tag{15}$$

The W^d is the un-mixing matrix estimated for D number of data sets i.e., $d = 1, 2, \ldots, D$. The un-mixed data vectors are represented as $y_1^d, y_2^d, \ldots, y_k^d$.

B. IVA BASED SIGNAL PROCESSING

The grounding grid signals are recorded in the presence of strong EMI signals. The total number of signals is denoted by K, each signal has data block length L with D number of data sets. The recorded mixed data contains D number of data sets $(X^1)^T, (X^2)^T, \ldots, (X^D)^T$. The task of the IVA algorithm is to estimate the source signals from the recorded mixed signals. The BSS algorithms know nothing except independence and non-Gaussianity of the source signals.

The IVA algorithm estimate the source signals as a first data set and their delayed versions as other data sets. This estimation is performed through minimization of the mutual information among the estimated source component vectors (SCVs). The cost function of IVA is demonstrated in [28] and discussed here as:

$$Q_{IVA} = \sum_{k=1}^{K} \Big(\sum_{d=1}^{D} H[y_k^d] - Q[y_k] \Big) - \sum_{d=1}^{D} \log \left| W^d \right| - C \tag{16}$$

The $Q[y_k]$ represents mutual information within k_{th} SCVs, H is the entropy, W^d is the un-mixing matrix of d_{th} data set, C is a constant factor which is equivalent to $H[X^1, X^2, \ldots, X^D]$, depending only on the recorded mixed data. The IVA algorithm minimizes the cost function in (16) and maximizes the mutual information within each SCV.

The IVA combines the advantages of CCA and ICA in a single framework. Variants algorithms of IVA exist in the literature are IVA-GGD, IVA-L and IVA-G [30] and their dominance is already proved. Motivated by this, we implemented IVA based grounding grid fault diagnosis. All these algorithms utilize the IVA cost function given in (16) to estimate the un-mixing matrices. The IVA-L utilize the HOS for un-mixing while ignoring the sample to sample dependency and SOS. Matrix gradient approach is used in the implementation of the IVA-L algorithm. Moreover, processing of the original as well as the delayed versions make the IVA algorithms more practical as compare to the ICA technique. Based on these advantages, IVA-L is used along the gradient method to diagnose faults in grounding grid considering the real substation environment.

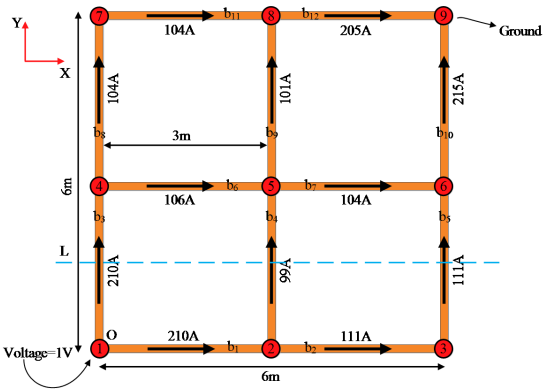

FIGURE 5. Squared mesh grounding grid of dimensions 6m×6m with mesh size 3m×3m. A potential of 1V is applied across node 1 and 9 to attain the flow of current. Arrows show the distribution of current where *L* is the line to measure the surface magnetic flux density.

IV. PERFORMANCE EVALUATION OF THE GRADIENT METHOD AND RESULTS ANALYSIS

The feasibility of the gradient method for the fault diagnosis of grounding grid is shown through simulations using COMSOL Multiphysics 5.0 [31] and Matlab. Magnetic flux density and electric field from the grounding grid is acquired through COMSOL Multiphysics while the IVA is implemented using Matlab.

A. THE NUMERICAL MODEL

A dimensions of 6m×6m squared mesh grid with mesh size of 3m×3m illustrated in Fig. 5 is modeled under the COMSOL Multiphysics 5.0 environment. This grid is made up of copper conductors of conductivity 5.998×10^7S/m and cross sectional area 5.024×10^{-5}m^2. It is buried 0.3m deep in a homogeneous soil of resistivity 100Ωm and permeability μ. Nodes are labeled from 1 to 9 and branches are represented as b_1 to b_{12}. To produce the surface magnetic flux density, a potential of 1V dc is applied across node 1 and 9. The flow of current in the grid is shown by arrows and value of current in each conductor is labeled.

To illustrate the performance of gradient method for the fault diagnosis of grounding grid. Firstly, the gradient method is applied to the normal grid illustrated in Fig. 5. 2^{nd} order

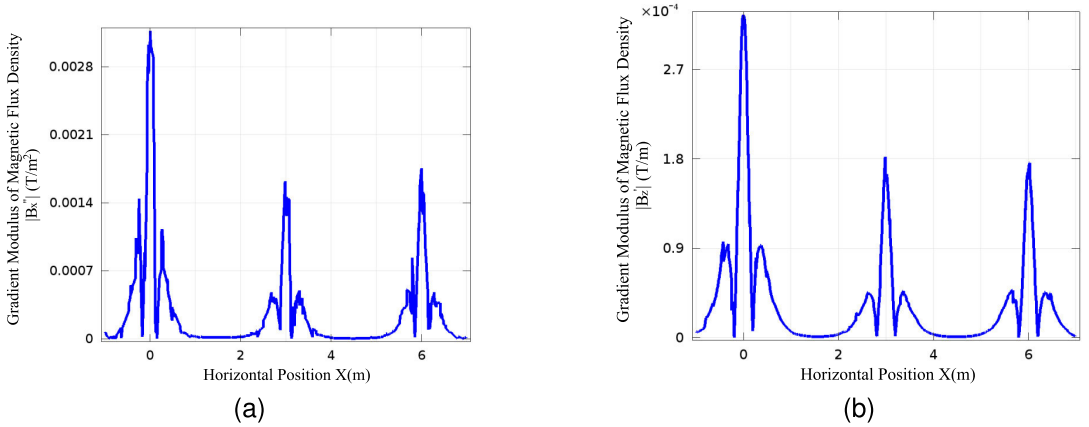

FIGURE 6. Gradient modulus of magnetic flux density on line L. Gradient peaks at 0m, 3m and 6m along the x-axis confirm the location of branches b_3, b_4 and b_5. (a) 2^{nd} order gradient modulus of $\vec{B_x}$. (b) 1^{st} order gradient modulus of $\vec{B_z}$.

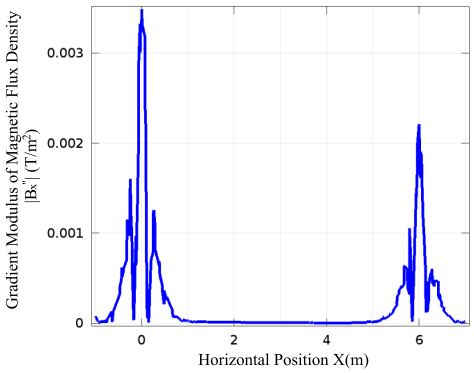

FIGURE 7. 2^{nd} order gradient modulus of $\vec{B_x}$. Two peaks at 0m and 6m along the x-axis confirm the branches b_3 and b_5 while the absence of peak at 3m confirms the branch b_4 as broken.

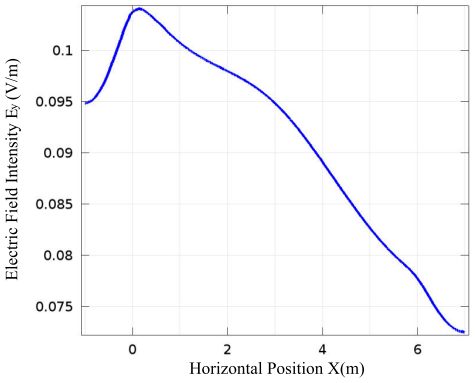

FIGURE 8. Electric field intensity $\vec{E_y}$ on line L.

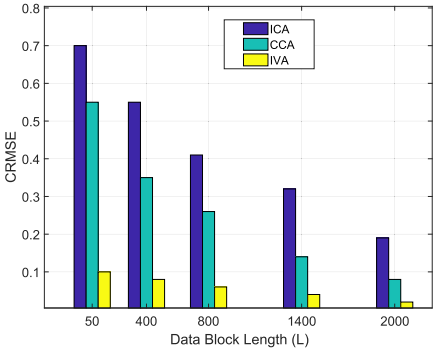

FIGURE 9. Comparison of the ICA, CCA and the IVA algorithms for EMI suppression in the grounding grid fault diagnosis.

gradient of the horizontal component $\vec{B_x}$ and 1^{st} order gradient of the vertical component $\vec{B_z}$ is taken along the line L. The results of $|\vec{B_x}''|$ and $|\vec{B_z}'|$ are shown in Fig. 6. Fig. 6a and 6b depict three peaks at 0m, 3m and 6m along the x-axis confirming the location of branches b_3, b_4 and b_5. Utilizing (7) to (10) the depth of the grid and current in the branches b_3, b_4 and b_5 are calculated from the gradient graphs illustrated in Table 1. Analysis of the results acquired from $\vec{B_x}$ and $\vec{B_z}$ shows that $\vec{B_x}$ delivers accurate results. The reason is the main peak width, which is the distance between two points on the main peak at which the value is 1% of the maximum value [29]. The lower is the main peak width higher is the accuracy of it. The main peak width of $|B_x''|$ from Fig. 6a is approximately 0.3m while the main peak width of $|B_z'|$ from Fig. 6b is approximately 0.4m. Moreover, the main peak width also affects the distance between main peak and side peak accordingly, which is represented by L_{x2} for the $\vec{B_x}$ and L_{z1} for the $\vec{B_z}$ in Table 1. It is illustrated in the table that $L_{x2} = 0.3$m is less than $L_{z1} = 0.38$m. Therefore, the $\vec{B_x}$ delivers accurate results compare to the $\vec{B_z}$.

To illustrate the fault diagnosis with the gradient method, let the branch b_3 be corroded such that its conductivity drops to 4.998×10^7S/m. Branch b_4 be broken and the conductivity of b_5 be dropped to 3.998×10^7S/m. Applying the same potential of 1V across node 1 and 9 and taking the gradient of the surface magnetic flux density on line L. The result is given in Fig. 7 that illustrates the absence of magnetic flux

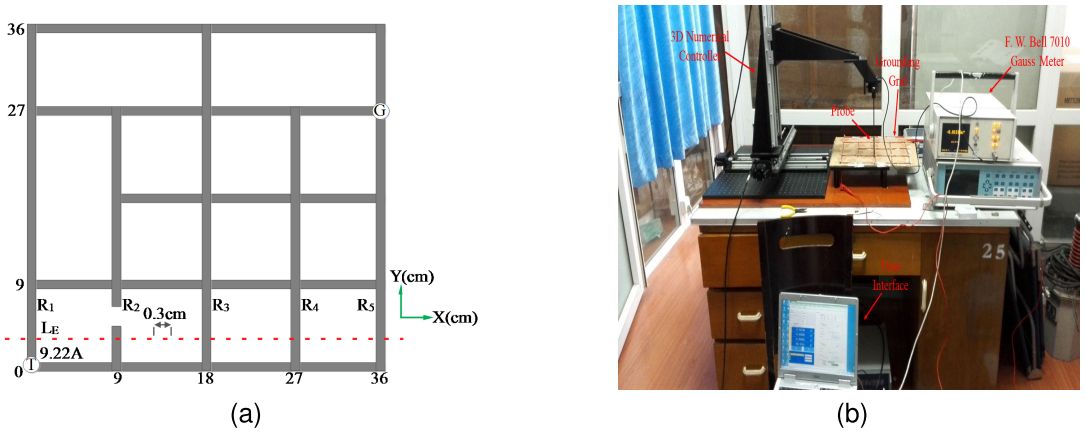

FIGURE 10. Lab test grounding grid model and experimental setup [32]. (a) 36cm×36cm grounding grid with mesh size 9cm. 9.2A dc is injected at *T* and *G* is grounded. L_E is the line of measurement and R_2 is the broken branch. (b) Experimental setup.

TABLE 1. Comparison between designed based and gradient method based characteristics of normal (faultless) grounding grid.

Function	L_{x2}	L_{z1}	Characteristic	Designed Based	Gradient Method Based
$\vec{B_x}$	0.3m	Nil	b_3 location (m)	0	0
			b_4 location (m)	3	3
			b_5 location (m)	6	6
			Depth h (m)	0.3	0.3
			b_3 current (A)	210	209.25
			b_4 current (A)	99	97.87
			b_5 current (A)	111	109
$\vec{B_z}$	Nil	0.38m	b_3 location (m)	0	0
			b_4 location (m)	3	3
			b_5 location (m)	6	6
			Depth h (m)	0.3	0.22
			b_3 current (A)	210	79
			b_4 current (A)	99	41
			b_5 current (A)	111	43

density gradient peak at 3m along the x-axis confirming the branch b_4 as broken. Contrarily, b_3 and b_5 are carrying the current evidenced by the presence of gradient peaks at 0m and 6m. However, to diagnose the corrosion in b_3 and b_5, (7) to (13) are utilized. To calculate the voltage drop across b_3 and b_5, electric field intensity is measured on line L. This is shown in Fig. 7. Table 2 lists the percentage corrosion in b_3 and b_5. In spite of the fact that FEM based software is open to noise due to their meshing property and the values are approximated, the conductivity calculated σ_c from the gradient method is in close approximation with the theoretical conductivity σ_t.

B. EXAMINING IVA FOR EMI SUPPRESSION

The presence of a variety of electrical and electronic equipment, switching operations and lightning strikes in the substation seeds its vicinity highly electromagnetic. These EM fields intermingle with the grounding grid signal at the receiving end acting as EM noise [33], [34]. EM noise comprises of the impulsive and continuous noise. The former includes noise due to switching and lightning while the latter include noise from the transformers, transmission lines, etc. This section illustrates the IVA performance considering the substation EM noise as a single unwanted signal. Single EM noise is considered for the sake that the IVA algorithm is independent of the character of noise as well as the number of noise (EM) signals. Therefore, increasing the EM signals does not affect the isolation performance of the IVA, rather the number of IVA sensors must be made equal to the number of EM signals.

Performance of the IVA-L algorithm of IVA is evaluated for the EMI suppression in the substation vicinity. SNRs ranging from 0 to 20dB are considered for the evaluation of IVA-L and results are compiled using Monte Carlo simulations. Furthermore, the number of source signals are $K = 2$, the number of data sets are $D = 4$, and various lengths L of the processing data blocks are considered in each data. Performance evaluation criteria considered are given below:

- Corresponding root mean square error (*CRMSE*) [35]:

$$CRMSE = \frac{RMS(s^d_{GG} - y^d_{GG})}{RMS(s^d_{GG})} \tag{17}$$

  The s^d_{GG} and y^d_{GG} represent the source grounding grid and the reconstructed grounding grid signals simultaneously at data set d.
- Common inter-symbol-interference (ISI_{com}) [28]:

$$ISI_{com} = \frac{1}{2K(K-1)}\left[\psi' + \psi''\right] \tag{18}$$

  where

$$\psi' = \sum_{n=1}^{K}\left(\sum_{m=1}^{K}\frac{g'_{m,n}}{max_p g'_{n,p}} - 1\right)$$

$$\psi'' = \sum_{m=1}^{K}\left(\sum_{n=1}^{K}\frac{g'_{m,n}}{max_p g'_{p,m}} - 1\right)$$

TABLE 2. Calculated resistivity and percentage corrosion from the magnetic flux density function $\vec{B_x}$.

Function	L_{x2} (m)	Branch	$\sigma_d \times 10^7$ (S/m)	$\sigma_t \times 10^7$ (S/m)	$\vec{E_y}$ (V/m)	$\sigma_c \times 10^7$ (S/m)	Corrosion$_{\%}$	Error$_{\%}$
$\vec{B_x}$	0.3	b_3	5.998	4.998	0.1038	4.62	22.97	7.56
		b_4	5.998	0.00	0.0949	0.00	Broken	0.00
		b_5	5.998	3.998	0.0777	3.80	36.64	4.95

TABLE 3. ISI_{com} of the IVA-L, FastICA and CCA for the L ranging from 50 to 2000 and SNR 20dB.

L	IVA-L	FastICA	CCA
50	0.10	0.60	0.47
100	0.057	0.12	0.09
500	0.053	0.08	0.071
1000	0.05	0.07	0.063
2000	0.05	0.06	0.055

TABLE 4. ISI_{com} of the IVA-L, FastICA and CCA for the SNR ranging from 0 to 20dB and $L = 2000$.

SNR (dB)	IVA-L	FastICA	CCA
0	0.873	0.96	0.90
5	0.533	0.85	0.79
10	0.157	0.34	0.28
20	0.05	0.06	0.055

and

$$g_{m,n} = \sum_{d=1}^{D} |g_{m,n}^{d}|$$
$$G^d = W^d A^d$$

The ISI_{com} is normalized so that its maximum value is one and minimum value is zero. The zero value corresponds to ideal separation performance.

Initially, the effectiveness of the IVA algorithm in comparison with the ICA and CCA techniques is demonstrated. Results of all the three techniques are illustrated in Fig. 9, taking into account the Fast-ICA algorithm [36] of ICA, the GMCA algorithm [37] of CCA and the IVA-L algorithm of the IVA. For *CRMSE*, SNR of 10dB is allowed. In case of ICA algorithm the value of data set is one. Performance evaluation is carried out for different values of L ranging from 50 to 2000 samples in a single data set. The simulation results clearly show that the IVA outperforms the ICA and CCA algorithms. The results also verify that the IVA algorithm is less sensitive to the processing data block lengths. The performance improvement of IVA at $L = 100$ is approximately 83% and CCA is 16% as compared to ICA.

Performance of the IVA-L algorithm is also investigated for various data block lengths. The ISI_{com} performance criteria is considered and the results are illustrated in Table 3. The data block lengths range from 50 to 2000 samples with SNR of 20dB. These results show that the IVA-L is less sensitive to the length of the processing data blocks as compared to ICA and CCA. Furthermore, the algorithm's performance is also evaluated for different SNR values with input data block length of 2000 samples in each data set. Results are given in Table 4 for SNR ranging from 0 to 20dB. Performance of the algorithms degrade for lower values of SNR. The IVA-L provide better results as compared to ICA and CCA for lower SNR values.

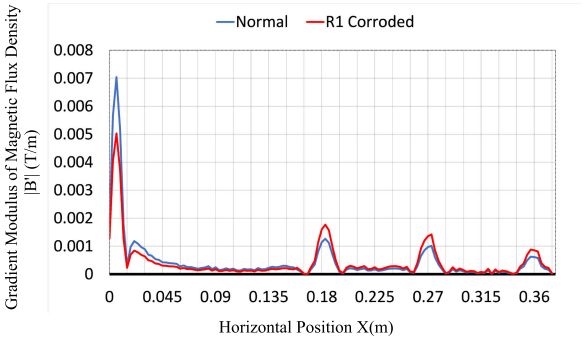

FIGURE 11. Gradient modulus of magnetic flux density on L_E. The absence of peak at 0.096m confirms R_2 as broken. The blue graph illustrates the magnetic flux density of the normal grounding grid while the red graph shows the magnetic flux density when R_1 is corroded.

V. EXPERIMENTAL AUTHENTICATION

The proposed method is authenticated via experimental testing. The grounding grid illustrated in Fig. 10a is constructed in lab that has dimensions of 36cm×36cm and mesh size 9cm. DC current of 9.2A is injected at the terminal T and the node G is grounded. Branch R_2 is considered as broken. Moreover, magnetic flux density is measured at a height of 1cm on line L_E. A total of 127 points are taken on L_E with adjacent points 0.3cm apart. Fig. 10b illustrates the test equipment where the probe of F. W. BELL 7010 Gauss meter is moved via a controller in three dimensions with an accuracy of 0.01mm [32].

The outcome of the gradient approach applied to the measurement on L_E is illustrated in Fig. 11. Here, peak at 0.006m, 0.183m, 0.273m and 0.36m corresponds to the branches R_1, R_3, R_4 and R_5. The peak corresponding to R_2 is absent, confirming R_2 as broken. The Fig. 11 depicts two cases, normal grounding grid and the branch R_1 corroded. This is shown by the blue and the red graph respectively. The depth of the grid and the current in R_1 is calculated using (8)-(10). The distance between main peak and side peak of R_1 is 0.015m in each case, therefore, the depth calculated is 9mm while the

current in R_1 is 4A approximately when the grid is normal. When R_1 is corroded the figure shows that the magnitude of the gradient magnetic flux density is reduced from 0.007T/m to 0.005T/m that equates the current in R_1 as 2.5A. Since, the current follows a low resistive path therefore, current has increased in the branch R_3, R_4 and R_5. This is illustrated by the increase in the magnetic flux density at the location of respective branches.

VI. CONCLUSION

Corroded grounding grid is an invisible danger to the safety of substation equipment and operators. In this paper, we have developed a new electromagnetic method to diagnose faults in grounding grid. In this method the status of the grounding conductors is determined by comparing the calculated resistivity with the designed resistivity. The resistivity is calculated using ohm's law. Therefore, the current in grounding conductor is determined from the surface magnetic flux density of the corresponding conductor while the voltage drop across it, is calculated from the surface electric field.

Due to the presence of electromagnetic equipment in the substation, the electromagnetic methods for grounding grid fault diagnosis are open to electromagnetic interference. To isolate the grounding grid signal from the interfered signal, we utilized the IVA. To investigate the viability of the IVA, the performance criterion such as *CRMSE* and ISI_{com} are taken into account. The *CRMSE* of IVA for $L = 50$ illustrated in Fig. 9 is approximately 84% low as compare to ICA and 81% as compare to CCA. This performance is almost independent of the data block length. Furthermore, the ISI_{com} of IVA for $L = 50$ illustrated in Table 3 is 83% low than the ICA. The results illustrate that the proposed electromagnetic method along the IVA is feasible to diagnose grounding grid faults under the EME of the substation.

As a future direction, we will test the performance of the proposed approach in the real substation.

REFERENCES

[1] Z. Fu, X. Wang, Q. Wang, X. Xu, N. Fu, and S. Qin, "Advances and challenges of corrosion and topology detection of grounding grid," *Appl. Sci.*, vol. 9, no. 11, p. 2290, Jun. 2019.

[2] *IEEE Guide for Safety in AC Substation Grounding–Redline*, IEEE Standard 80-2013 (Revision IEEE Standard 80-2000/ Incorporates IEEE Standard 80-2013/Cor 1-2015)-Redline, 2015, pp. 1–426.

[3] R. Alipio, M. A. O. Schroeder, and M. M. Afonso, "Voltage distribution along Earth grounding grids subjected to lightning currents," *IEEE Trans. Ind. Appl.*, vol. 51, no. 6, pp. 4912–4916, Nov. 2015.

[4] Y. He, X. Shao, J. Hu, Y. Liu, C. Jin, and J. Pan, "Corrosion condition detect of entire grounding system in a 500 kV converting station using electrical impedance imaging method," in *Proc. IEEE Int. Conf. High Voltage Eng. Appl. (ICHVE)*, Sep. 2018, pp. 1–4.

[5] X. Li, F. Yang, J. Ming, A. Jadoon, and S. Han, "Imaging the corrosion in grounding grid branch with inner-source electrical impedance tomography," *Energies*, vol. 11, no. 7, p. 1739, Jul. 2018.

[6] K. Liu, F. Yang, X. Wang, B. Gao, X. Kou, M. Dong, and A. Jadoon, "A novel resistance network node potential measurement method and application in grounding grids corrosion diagnosis," *Prog. Electromagn. Res. M*, vol. 52, pp. 9–20, 2016.

[7] F. Yang, Y. Wang, M. Dong, X. Kou, D. Yao, X. Li, B. Gao, and I. Ullah, "A cycle voltage measurement method and application in grounding grids fault location," *Energies*, vol. 10, no. 11, p. 1929, Nov. 2017.

[8] Y. Shao, M. Mu, B. Zhang, K. Nie, and Q. Liao, "Corrosion behavior of copper-clad steel bars with unclad two-end faces for grounding grids in the red clay soil," *J. Mater. Eng. Perform.*, vol. 26, no. 4, pp. 1751–1757, Apr. 2017.

[9] J. Li, H. Su, F. Chai, D.-M. Xue, L. Li, X.-Y. Li, and H.-M. Meng, "Corrosion behavior of low-carbon Cr micro-alloyed steel for grounding grids in simulated acidic soil," *J. Iron Steel Res. Int.*, vol. 25, no. 7, pp. 755–766, Jul. 2018.

[10] X.-L. Zhang, X.-H. Zhao, Y.-G. Wang, and N. Mo, "Development of an electrochemical *in situ* detection sensor for grounding grid corrosion," *Corrosion*, vol. 66, no. 7, 2010, Art. no. 076001.

[11] P.-H. Zhang, J.-J. He, D.-D. Zhang, and L.-M. Wu, "A fault diagnosis method for substation grounding grid based on the square-wave frequency domain model," *Metrol. Meas. Syst.*, vol. 19, no. 1, pp. 63–72, Jan. 2012.

[12] L. Kai, Y. Fan, Z. Songyang, Z. Liwei, H. Jiayuan, W. Xiaoyu, and I. Ullah, "Research on grounding grids imaging reconstruction based on magnetic detection electrical impedance tomography," *IEEE Trans. Magn.*, vol. 54, no. 3, pp. 1–4, Mar. 2018.

[13] A. Qamar, N. Shah, Z. Kaleem, Z. Uddin, and F. A. Orakzai, "Breakpoint diagnosis of substation grounding grid using derivative method," *Progr. Electromagn. Res. M*, vol. 57, pp. 73–80, 2017.

[14] S. Qin, Y. Wang, Z. Xu, X. Liao, L. Liu, and Z. Fu, "Fast resistivity imaging of transient electromagnetic using ANN," *IEEE Geosci. Remote Sens. Lett.*, vol. 16, no. 9, pp. 1373–1377, Sep. 2019.

[15] C. Yu, Z. Fu, Q. Wang, H.-M. Tai, and S. Qin, "A novel method for fault diagnosis of grounding grids," *IEEE Trans. Ind. Appl.*, vol. 51, no. 6, pp. 5182–5188, Nov./Dec. 2015.

[16] X. Li, F. Yang, J. Ming, A. Jadoon, and S. Han, "Imaging the corrosion in grounding grid branch with inner-source electrical impedance tomography," *Energies*, vol. 11, no. 7, p. 1739, Jul. 2018.

[17] F. Yang, Y. Wang, M. Dong, X. Kou, D. Yao, X. Li, B. Gao, and I. Ullah, "A cycle voltage measurement method and application in grounding grids fault location," *Energies*, vol. 10, no. 11, p. 1929, Nov. 2017.

[18] J. Jordana, M. Gasulla, and R. Pallàs-Areny, "Electrical resistance tomography to detect leaks from buried pipes," *Meas. Sci. Technol.*, vol. 12, no. 8, p. 1061, 2001.

[19] X. Wang, Z. Fu, Y. Wang, R. Liu, and L. Chen, "A non-destructive testing method for fault detection of substation grounding grids," *Sensors*, vol. 19, no. 9, p. 2046, May 2019.

[20] B. Z. Jinliang He and R. Zeng, *Methodology and Technology for Power System Grounding*. Singapore: Wiley, 2013.

[21] A. K. Maddirala and R. A. Shaik, "Separation of sources from single-channel eeg signals using independent component analysis," *IEEE Trans. Instrum. Meas.*, vol. 67, no. 2, pp. 382–393, Feb. 2018.

[22] A. Qamar, Z. Uddin, and F. Yang, "Inverse features extraction for substation grounding grid: Derivative and ICA combinatorial approach," *IET Gener., Transmiss. Distrib.*, vol. 13, no. 24, pp. 5457–5466, Dec. 2019.

[23] E. Urrestarazu, J. Iriarte, M. Alegre, M. Valencia, C. Viteri, and J. Artieda, "Independent component analysis removing artifacts in ictal recordings," *Epilepsia*, vol. 45, no. 9, pp. 1071–1078, 2004.

[24] A. J. Shackman, B. W. McMenamin, H. A. Slagter, J. S. Maxwell, L. L. Greischar, and R. J. Davidson, "Electromyogenic artifacts and electroencephalographic inferences," *Brain Topogr.*, vol. 22, no. 1, pp. 7–12, Feb. 2009.

[25] W. De Clercq, A. Vergult, B. Vanrumste, W. Van Paesschen, and S. Van Huffel, "Canonical correlation analysis applied to remove muscle artifacts from the electroencephalogram," *IEEE Trans. Biomed. Eng.*, vol. 53, no. 12, pp. 2583–2587, Nov. 2006.

[26] R. Mowla, S.-C. Ng, M. S. A. Zilany, and R. Paramesran, "Artifacts-matched blind source separation and wavelet transform for multichannel EEG denoising," *Biomed. Signal Process. Control*, vol. 22, pp. 111–118, Sep. 2015.

[27] M. Anderson, G.-S. Fu, R. Phlypo, and T. Adali, "Independent vector analysis: Identification conditions and performance bounds," *IEEE Trans. Signal Process.*, vol. 62, no. 17, pp. 4399–4410, Sep. 2014.

[28] M. Anderson, T. Adalı, and X.-L. Li, "Joint blind source separation with multivariate Gaussian model: Algorithms and performance analysis," *IEEE Trans. Signal Process.*, vol. 60, no. 4, pp. 1672–1683, Apr. 2012.

[29] Y. Fan, L. Kai, Z. Liwei, Z. Songyang, H. Jiayuan, W. Xiaoyu, and G. Bin, "A derivative-based method for buried depth detection of metal conductors," *IEEE Trans. Magn.*, vol. 54, no. 4, pp. 1–9, Apr. 2018.

[30] T. Kim, H. T. Attias, S.-Y. Lee, and T.-W. Lee, "Blind source separation exploiting higher-order frequency dependencies," *IEEE Trans. Audio, Speech Lang. Process.*, vol. 15, no. 1, pp. 70–79, Jan. 2007.

[31] *AC/DC Module User's Guide, version 5.0*. COMSOL. Accessed: Jul. 2017. [Online]. Available: http://www.comsol.com
[32] A. Qamar, F. Yang, W. He, A. Jadoon, M. Z. Khan, and N. Xu, "Topology measurement of substation's grounding grid by using electromagnetic and derivative method," *Prog. Electromagn. Res. B*, vol. 67, pp. 71–90, 2016.
[33] M. Au, F. Gagnon, and B. Agba, "An experimental characterization of substation impulsive noise for a RF channel model," in *Proc. PIERS*, 2013, pp. 1–6.
[34] H. Li, L. Liu, Y. Li, Z. Yuan, and K. Zhang, "Measurement and characterization of electromagnetic noise in edge computing networks for the industrial Internet of Things," *Sensors*, vol. 19, no. 14, p. 3104, Jul. 2019.
[35] X. Chen, H. Peng, F. Yu, and K. Wang, "Independent vector analysis applied to remove muscle artifacts in EEG data," *IEEE Trans. Instrum. Meas.*, vol. 66, no. 7, pp. 1770–1779, Jul. 2017.
[36] Z. Uddin, A. Ahmad, and M. Iqbal, "ICA based MIMO transceiver for time varying wireless channels utilizing smaller data blocks lengths," *Wireless Pers. Commun.*, vol. 94, no. 4, pp. 3147–3161, Jun. 2017.
[37] Y.-O. Li, T. Adalı, W. Wang, and V. D. Calhoun, "Joint blind source separation by multiset canonical correlation analysis," *IEEE Trans. Signal Process.*, vol. 57, no. 10, pp. 3918–3929, Oct. 2009.

AAMIR QAMAR received the Ph.D. degree in electrical engineering from Chongqing University, China, in 2016. During his Ph.D., he was with the State and Key Laboratory of Power Transmission and System Security and New Technology, Chongqing University. His research interests include signal processing and electromagnetic. He is currently working on the performance analysis of substation grounding grid and the fault localization of underground cables.

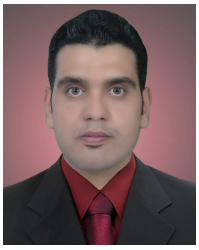

IBRAHIM H. AL-KHARSAN received the B.Eng. degree in electrical engineering from the University of Kufa, Najaf, Iraq, in 2008, the master's degree in engineering science from Jawaharlal Nehru Technological University Hyderabad, College of Engineering, India, in 2013, and the Ph.D. degree in electrical engineering from the Electrical Engineering Department, College of Engineering, Basrah University, Iraq, in 2020. He worked as a Lecturer with the College of Engineering, Kufa University; the Computer Technique's Department, Al-Kadhum University College; and the Electrical Department, Al-Najaf Institute, that related to Al-Furat Al-Awsat Technical University. He is currently a Lecturer with the Computer Technique's Department, College of Technical Engineering, Islamic University.

ZAHOOR UDDIN received the degree in industrial electronics engineering from the NED University of Engineering and Technology, Pakistan, in 2003, the M.S. degree in electronics from Air University Islamabad, Pakistan, in 2008, and the Ph.D. degree in signal processing and communication from the COMSATS Institute of Information Technology, Wah Campus, Pakistan, in 2016. He is currently a Faculty Member with the Department of Electrical and Computer Engineering, COMSATS University Islamabad, Wah Campus. His research interests include algorithms and applications of blind source separation in various fields, analog and digital signal processing, and instrumentation.

AHMED ALKHAYYAT received the B.Sc. degree in electrical engineering from Al Kufa University, Najaf, Iraq, in 2007, the M.Sc. degree from the Dehradun Institute of Technology, Dehradun, India, in 2010, and the Ph.D. degree from Cankaya University, Ankara, Turkey, in 2015. He is currently the Dean of international relationship and manager of the word ranking with Islamic University, Najaf, Iraq. His research interests include the IoT in the health-care systems, SDN, network coding, cognitive radio, efficient-energy routing algorithms, and efficient-energy MAC protocol in cooperative wireless networks and wireless body area networks, as well as cross-layer designing for self-organized networks. He contributed in organizing a several IEEE conferences, workshop, and special sessions. To serve his community, he acted as a reviewer for several journals and conferences.